Seismic diffraction imaging to better characterise mass-transport complexes: examples from the Gulf of Cadiz, south west Iberian Margin

This manuscript is a non-peer reviewed pre-print submitted to EarthArXiv. The manuscript has been submitted for publication in Journal of Geophysical Research: Solid Earth. If accepted, the final version of this manuscript will be available via the Peer-reviewed Publication DOI link on the right-hand side of this webpage.

Please feel free to contact any of the authors, we welcome feedback:

Jonathan Ford[1,2] (jford@inogs.it)
Roger Urgeles[3] (urgeles@icm.csic.es)
Angelo Camerlenghi[1] (acamerlenghi@inogs.it)
Eulàlia Gràcia[3] (egracia@icm.csic.es)

[1]National Institute of Oceanography and Applied Geophysics (OGS)
[2]University of Trieste
[3]Institut de Ciències del Mar (CSIC)

Seismic diffraction imaging to better characterise mass-transport complexes: examples from the Gulf of Cadiz, south west Iberian Margin

Jonathan Ford[1,2], Roger Urgeles[3], Angelo Camerlenghi[1], Eulàlia Gràcia[3]

[1]National Institute of Oceanography and Applied Geophysics - OGS
[2]University of Trieste
[3]Institut de Ciències del Mar, CSIC

Key Points:

- Diffracted energy in seismic reflection profiles can be used to image the fine-scale internal structure of mass-transport complexes
- Diffraction images allow better estimation of the runout of thin mass-transport complexes compared to conventional reflection images
- Out-of-plane diffractions may be used to estimate a minimum bound on the width of heterogeneous geobodies from a 2-D seismic profile

Corresponding author: Jonathan Ford, `jford@inogs.it`

Abstract

Mass-transport complexes are characterised by complex, laterally discontinuous internal structure, such as pressure ridges, local shear zones and intact translated blocks. Their internal structure is often poorly imaged by seismic reflection techniques, which are fundamentally limited in lateral resolution by the bandwidth of the seismic source. Diffraction imaging, instead, directly images subsurface heterogeneity by primarily imaging the diffracted part of the seismic wavefield. We apply seismic diffraction imaging to two marine multi-channel seismic profiles containing mass-transport complexes from the Gulf of Cadiz (south west Iberian Margin). We observe that mass-transport complexes generate a large amount of diffracted energy relative to the un-failed sediments. We demonstrate that, in combination with conventional seismic reflection images, diffraction images can be used to better discriminate the lateral extent (runout) of mass-transport complexes, particularly for thin bodies that are not well-resolved using conventional imaging. We suggest that diffraction imaging may have similar applications for marine geohazard assessment to seismic discontinuity attributes, such as the similarity attribute, with the advantage of being closer to a true image of the heterogeneous subsurface. Applying diffraction imaging to image mass-transport complexes from 2-D seismic data is challenging, but may provide some unique insights that are not available from conventional reflection images.

1 Introduction

Mass-transport complexes are the depositional record of subaqueous mass-failures, which include typologies such as debris flows, glides and slumps (Prior et al., 1984; Mulder & Cochonat, 1996; Piper et al., 1997; Sawyer et al., 2009). Marine geophysical techniques to characterise such deposits are increasingly important for societal, industrial and scientific applications. Subaqueous mass-failures events pose significant geohazard to coastal populations from landslide-induced tsunami (Tappin et al., 2001; Satake, 2012) and may threaten seafloor infrastructure such as telecommunications cables, wind farms and pipelines (Piper et al., 1999; Carter et al., 2014). Mass-transport complexes have implications for hydrocarbon exploration as they form a significant proportion of deep-water sediment fill and can have both reservoir and seal potential (Weimer & Shipp, 2004; Alves et al., 2014; Cardona et al., 2016). They also represent a drilling hazard as they are often over-consolidated (densified) compared to un-failed sediments (Shipp et al., 2004).

In recent years there has been an increased focus on using seismic reflection data to image mass-transport complexes to better understand the parameters that control their emplacement and transport (e.g., Moscardelli & Wood, 2008; Bull et al., 2009; Posamentier et al., 2011; Steventon et al., 2019). Such parameters include runout velocity, flow acceleration/confinement and flow type, which have a strong influence on the geohazard potential of an event. Seismic reflection data are well-suited to delineate the external geometry of the resulting bodies as they often have an erosional basal shear surface and a non-conformal upper surface, which tend to produce high-amplitude, laterally coherent bounding seismic reflections. The mapped extent (runout) is used to back-calculate physical properties of the flow, and is often the only data available to assess the dynamic evolution (velocity and acceleration) of submarine slope failures and resulting tsunamis (e.g., De Blasio et al., 2003; Løvholt et al., 2017). Outcrop studies have shown that mass-transport complexes can preserve strongly deformed and heterogeneous internal structure (Lucente & Pini, 2003; Sobiesiak et al., 2017). Such structure requires high lateral resolution to properly image in seismic data. Reflection images, however, have inherently limited lateral resolution according to the Rayleigh criterion: approximately half the dominant seismic wavelength (Born & Wolf, 1959) or on the order of tens of metres for conventional multi-channel marine seismic data near the seafloor (Chen & Schuster, 1999). As a result, conventional seismic images of mass-transport complexes often show apparent "chaotic" or "transparent" seismic texture (Bull et al., 2009). It is difficult to determine if such texture is representative of the true geology or simply due to inadequate resolution.

Specular seismic reflections are generated by impedance contrasts across smooth, laterally continuous subsurface interfaces. Seismic diffractions, instead, are generated by geological structure that is laterally heterogeneous around or below the scale of the seismic wavelength (on the order of 10 m to 100 m for conventional multi-channel seismic data; Khaidukov et al., 2004). Classic examples of structures that may generate diffractions include faults, channels, pinchouts, rugose interfaces and vertical fractures (Fomel et al., 2007; Reshef & Landa, 2009). Diffractions are visible in unmigrated seismic images as so-called *diffraction tails*. These can be one-sided, in the case of lateral truncations, or two-sided (so-called *diffraction hyperbolae*) in the case of point diffractors.

Diffraction imaging works by separating the reflected and diffracted wavefields and migrating only the diffracted component (e.g., Khaidukov et al., 2004; Fomel et al., 2007;

Moser & Howard, 2008; Decker et al., 2017; Schwarz, 2019). Migration can properly image diffractions by collapsing the diffraction tails back to their origin point, producing an image of the heterogeneous subsurface. Contrary to specular reflections, the diffracted wavefield can encode subsurface information at a scale below the limit of the Rayleigh criterion (Khaidukov et al., 2004). Bachrach and Reshef (2010) demonstrate that visible diffractions can be generated by an object much smaller than the wavelength of the seismic source, provided there is a sufficiently large impedance contrast and adequate spatial sampling of receivers. This means that diffraction imaging has the potential to provide "super-resolution" of geological structure, beyond the resolution of conventional reflection images.

We suggest that, compared to un-failed sediments, mass-transport complexes should contain a large amount of *diffraction generators*: laterally discontinuous, metre- to decametre-scale internal structure created by transport and emplacement processes. Examples of such structure include small-scale faulting and folding; transported or remnant mega-clasts; vertical fluid escape structures; headwall scarps; pressure ridges and ramp-and-flat structures (Lucente & Pini, 2003; Diviacco et al., 2006; Moscardelli & Wood, 2008; Bull et al., 2009; Alves & Lourenço, 2010; Sobiesiak et al., 2017). Such structure may be below the resolution limit of specular reflections, but may still generate diffractions provided there is a sufficient impedance contrast preserved after emplacement.

In this paper we aim to assess the potential of diffraction imaging to better image the discontinuous internal structure of mass-transport complexes. We apply diffraction imaging to two multi-channel 2-D seismic profiles containing prominent mass-transport complexes from the Gulf of Cadiz (south west Iberian Margin) in order to:

1. assess the ability to resolve heterogeneous internal structure compared to conventional seismic reflection images.
2. compare diffraction images to conventional seismic discontinuity attributes for delineating relatively small and thin heterogeneous bodies.
3. demonstrate how out-of-plane diffracted energy may be used to constrain the 3-D structure of strongly heterogeneous bodies using 2-D seismic profiles.

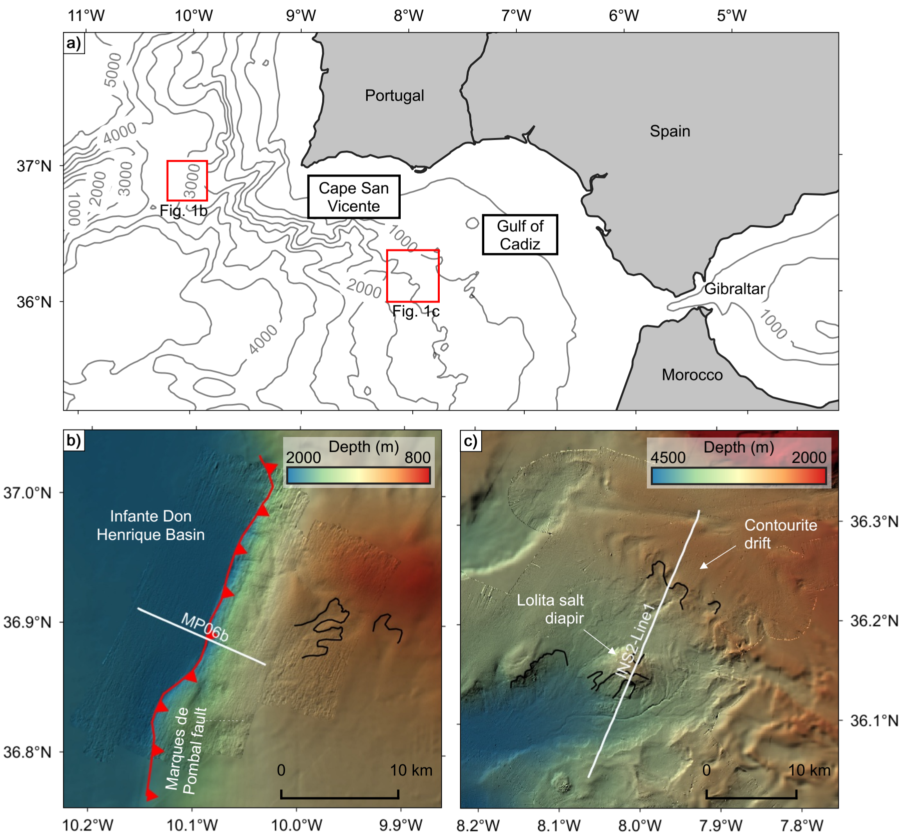

Figure 1. a) Overview map of the Gulf of Cadiz and surroundings, with bathymetric contours (500 m interval). b) Infante Don Henrique Basin area, location of Marquês de Pombal fault trace and seismic profile MP06b indicated (after Lo Iacono et al., 2012). c) Bathymetry of Portimão Bank area, location of seismic profile INS2-Line1 indicated. Headscarps are shown in black.

Diffraction separation and imaging is an established geophysical technique to image heterogenous geology using seismic data. To the authors' knowledge, this is the first published example of diffraction imaging applied to characterise mass-transport complexes.

2 Geological Setting

The Gulf of Cadiz is located offshore the south west margin of the Iberian Peninsula and north west Morocco (Fig. 1). The region is characterised by active tectonics related to convergence between the African and Eurasian plates. The tectonic structure and seafloor morphology of the gulf is the result of an accretionary wedge that formed from the Late Cretaceous to the Late Miocene (Zitellini et al., 2009). The accretionary wedge is covered by Late Miocene to Plio-Quaternary sediments, pierced by mud volcanoes and pockmarks, which indicate active fluid flow, and salt diapirs (Gràcia, Dañobeitia, Vergés, Bartolomé, & Córdoba, 2003; Gràcia, Dañobeitia, Vergés, & Team, 2003; Zitellini et al., 2009; Medialdea et al., 2009). The Gulf of Cadiz and the south west Iberian Margin host large magnitude ($M_w > 8$) earthquakes (Gràcia et al., 2010; Matias et al., 2013) and submarine landslides (Urgeles & Camerlenghi, 2013). There is significant hazard to coastal populations from tsunami associated with both processes (M. A. Baptista & Miranda, 2009; Lo Iacono et al., 2012; Leynaud et al., 2017). This study focuses on geophysical data collected from two areas of the Gulf of Cadiz: the Portimão Bank and the Infante Don Henrique Basin.

The Portimão Bank is located south of Portugal, at the external part of the Gulf of Cadiz between 9°W to 8°20′W and 36°N to 36°20′N. The Portimão Bank is an east-west trending tectonic high characterised by bottom currents and contourite deposition associated with the Mediterranean Outflow Water (Brackenridge et al., 2013) and mass movements (slides and slide scars). Salt diapirs pierce the shallow Plio-Quaternary sediments and the corresponding doming is evident in the bathymetry (Fig. 1). The rapid deposition of poorly consolidated contourites and slope steepening from salt diapirism are primary pre-conditioning factors for mass-failure, evidence of which is widespread in the area. As for the whole south west Iberian Margin, the Portimão Bank area is seismically active, providing a potential trigger mechanism for the observed mass-failures.

The Infante Don Henrique Basin is located at the south west of the Cape São Vicente (Fig. 1). It is bound on its eastern side by the Marquês de Pombal fault, an approximately 55 km long, north-south trending, active reverse thrust fault (Gràcia, Dañobeitia, Vergés, Bartolomé, & Córdoba, 2003; Terrinha et al., 2003; Zitellini et al., 2004). The fault is expressed in the bathymetry as a monocline, with water depth rapidly increasing from the hanging-wall block (2000 m water depth) to the basin located in the footwall block (3900 m water depth). Within the Infante Don Henrique Basin there is a succession of stacked mass-transport complexes preserved in the Plio-Quaternary deposits. It is likely that this accumulation of mass-transport deposits record the recent seismic activity of the fault (Vizcaino et al., 2006). Recent mass-failure events are also visible in the bathymetry of the steeply dipping hanging wall block (Fig. 1b). The Marquês de Pombal fault has been considered as a potential source of the $M_w > 8$ 1755 Lisbon earthquake (M. Baptista et al., 1998). It has also been hypothesised that a submarine landslide on the slope may have contributed to the resulting tsunami. Preconditioning factors for mass-failure in the area include slope steepening of the advancing thrust front and potential excess pore pressure related to the relatively high sedimentation rate and lateral fluid flow. Near-field seismic activity along the Marquês de Pombal fault is likely a primary trigger mechanism for some of the mass-failure events, as well as far-field seismicity from the rest of the Gulf of Cadiz.

3 Data and Methods

3.1 Geophysical Data

This study uses two multi-channel seismic reflection profiles from the Gulf of Cadiz acquired during the INSIGHT (Imaging large seismogenic and tsunamigenic structures of the Gulf of Cadiz with ultra-high resolution technologies) cruises in May 2018 (Leg 1) and October 2019 (Leg 2) (Gràcia et al., 2018; Urgeles et al., 2019).

The seismic acquisition and processing flow were designed to maximise the temporal and spatial resolution of the resulting seismic images. The shot interval was chosen to ensure a nominal coverage of at least 12-fold with a midpoint interval of 3.125 m. A relatively small seismic source (an airgun array with total volume 930 cu. in.) was used to maximise the dominant source frequency. The source array and streamer were towed at a relatively shallow depth (approximately 3 m) to ensure that the frequency of the first source and receiver ghost notches was as high as possible. Detailed acquisition parameters for the two profiles are given in Table 1. Broadband pre-processing was performed onboard using RadExPro seismic processing software. Traditional pre-processing focuses on imaging specular reflections, meaning that diffractions are often ignored or removed. Preserving diffractions through the pre-processing flow requires care as diffraction tails are generally lower amplitude, higher frequency and dip more steeply compared to reflections. The broadband pre-processing flow consisted of i) swell noise removal (to enhance the signal-to-noise ratio at low frequencies); ii) deghosting (to correct for the source and receiver ghost effect); iii) designature (to transform the data to zero-phase and remove the bubble pulse, boosting the low frequency content) and iv) shot domain $\tau - p$ muting (to remove steeply dipping noise). For most of the survey area, the signal penetration depth was similar to, or less than, the two-way travel time (TWTT) of the first waterbottom multiple, therefore no multiple attenuation was performed. Instead, a bottom-mute was applied from above the first waterbottom multiple before imaging to prevent

Table 1. Acquisition parameters for multi-channel seismic profiles MP06b and INS2-Line1

	Seismic profile	
	MP06b	INS2-Line1
Vessel	B/O Sarmiento de Gamboa	
Acquisition date	May 2018	October 2019
Profile length	11.6 km	32.2 km
Seismic source	Airgun array (10 × G-Gun II, 930 cu. in. total volume)	
Source depth	3.5 m	
Shot interval	18.5 m	12.5 m
Recording array	Solid-state digital streamer (GeoEel Geometrics)	
Receiver groups	72	56
Receiver group interval	6.25 m	
Streamer depth	3.5 m	
Near offset	104.9 m	
Far offset	548.75 m	448.65 m
Record length	8.0 s	5.8 s
Acquisition sample interval	0.5 ms	
Nominal coverage	12-fold	14-fold

high-amplitude multiple energy from migrating into the shallow section as noise. Full details of the broadband pre-processing flow are given in Table 2. Details of the seismic imaging performed after pre-processing are given in Section 3.2.3. The signal bandwidth of the resulting images is approximately 8 Hz to 250 Hz (range estimated from the amplitude spectrum of a window around the waterbottom reflection, 20 dB below the peak amplitude).

3.2 Diffraction Imaging

Seismic diffraction imaging aims to image the heterogeneous subsurface, as opposed to reflection imaging which primarily images smooth, laterally continuous interfaces. Diffraction imaging works by separating the specular reflected and diffracted wavefields and migrating only the separated diffractions. We perform the separation and imaging using

Table 2. Outline of the broadband pre-processing flow for multi-channel seismic profiles MP06b and INS2-Line1

Resample to 1 ms (anti-alias filter: 380–450 Hz high cut)
Remove recording delay (50 ms)
Navigation and geometry import
Trace editing (drop bad shots)
Swell noise attenuation (2–4 Hz low-cut filter, time-frequency trim in shot domain (2–40 Hz) and channel domain (2–20 Hz))
Source and receiver ghost removal (SharpSeis de-ghost; Vakulenko et al., 2014)
Designature (de-bubble filter and zero-phase correction, operator derived by stacking waterbottom reflection)
Shot domain $\tau - p$ mute (passing range $-200 < p < 400$ μs m^{-1})
CMP binning (3.125 m interval)

the open-source geophysics processing framework *Madagascar* (Fomel et al., 2013). An outline of the diffraction imaging workflow is given in Fig. 2.

3.2.1 Dip Estimation

This study uses a dip-guided plane-wave destruction filter (PWD) approach (Claerbout, 1992; Fomel, 2002) to eliminate reflection energy from common-offset, unmigrated data (Section 3.2.2). Proper diffraction separation, therefore, depends on accurate estimation of the local dip of the unmigrated reflections. The data analysed in this study contain a large amount of high-amplitude diffraction hyperbolae due to the general rough topography of the seafloor. In addition, some reflections are steeply dipping, often sub-parallel to the diffraction hyperbolae. This prevents accurate estimation of the dip of reflectors directly from unmigrated data (e.g., Fomel et al., 2007).

For this study, we instead estimate the local dip from the migrated image, then demigrate the dip field to estimate the local dip of the unmigrated data. First, we migrate the data using a pre-stack time migration (Section 3.2.3), collapsing the diffraction hyperbolae and enhancing the continuity of reflections. Then we estimate the local dip field of the migrated image by PWD, with lateral and vertical smoothing. The dip field is then

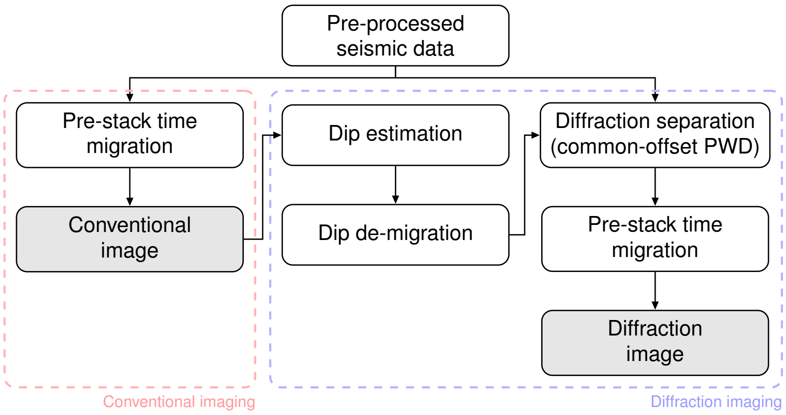

Figure 2. Diffraction imaging and conventional seismic reflection imaging workflows. The local dip field is estimated from a migrated image, then de-migrated using the migration velocities (Appendix A).

de-migrated using the migration velocities (Appendix A), giving a local dip field that approximates the unmigrated dip.

3.2.2 Diffraction Separation

For diffraction separation we treat the recorded seismic wavefield as being composed of i) specular reflections, ii) diffracted energy and iii) noise (including other seismic arrivals). If the noise is small, we can retrieve the diffracted wavefield by eliminating the specular reflections. We perform the separation using a dip-guided PWD approach on common-offset gathers (Claerbout, 1992; Fomel, 2002; Fomel et al., 2007). This approach assumes that for unmigrated, common-offset seismic data specular reflections are laterally coherent events with continuously varying slope (i.e., smooth). PWD filters can predict smooth, laterally continuous energy that is close to the estimated local dip. This approximates the specular reflected wavefield. We subtract this from the pre-processed, unmigrated, common-offset data to eliminate the reflections. The remaining data contains the diffracted wavefield, noise and some residual reflection energy.

3.2.3 Seismic Imaging

Diffractions are predicted by the wave equation, therefore diffractions can be imaged (like reflections) by any migration scheme derived from the wave equation. This includes Kirchhoff-type migrations, in both time and depth domains (Moser & Howard, 2008). For this study, all migrations are performed using a 2-D pre-stack Kirchhoff time migration (Lumley et al., 1994; Fomel et al., 2013), with a maximum migration angle of 60 degrees. Identical migrations are performed for the conventional and diffraction images so that the geometry of both images is comparable.

The seismic profiles analysed for this study were acquired using a short streamer (approximately 500 m far offset) compared to the water depth (>1 km), so there is no significant differential moveout of reflection events in common-midpoint domain to perform a robust semblance-based velocity analysis. Instead, the migration velocity field is modelled as a constant velocity in the water column and a velocity gradient in the sediments. The water velocity for both profiles is $1500\,\mathrm{ms}^{-1}$. The post-migration waterbottom horizon is picked on a near-offset section migrated with a water velocity $f-k$ migration (Stolt, 1978). The sediment velocity gradient is then inserted below the smoothed post-migration waterbottom horizon to make the migration velocity field. The optimal sediment velocity gradient is estimated by generating an ensemble of images migrated with a range of gradients and choosing the gradient that appeared to best image sediments along the whole profile. For seismic profiles INS2-Line1 and MP06b the optimal sediment velocity gradient was estimated onboard as $200\,\mathrm{ms}^{-2}$ and $125\,\mathrm{ms}^{-2}$, respectively.

3.3 Seismic Attributes

Seismic attributes highlight textural characteristics of the seismic image and help to discriminate between seismic facies (Chopra & Marfurt, 2007). Seismic discontinuity attributes can be used to delineate mass-transport complexes, which often show a disordered character compared to un-failed sediments (e.g, Bull et al., 2009; Alves et al., 2014; Bhatnagar et al., 2019).

The *similarity* attribute is a post-stack seismic attribute that measures the lateral similarity of adjacent traces, which has the effect of highlighting discontinuities in a seismic image (Randen & Sønneland, 2005). It is primarily used to map geological features characterised by discontinuous seismic reflectors, for example faults, gas chimneys and salt bodies. A similarity equal to 1 indicates a perfect match between adjacent traces within the time gate. Conversely, a similarity equal to 0 indicates no match. For this study we use the similarity attribute implementation from OpendTect 6.4 with a time gate of 10 ms.

We also use the average energy attribute to highlight areas with consistently high amplitudes in the diffraction image. The *average energy* attribute is a measure of average sample amplitude within a time window, highlighting lateral variation in trace amplitude. Average energy E at time t is defined as

$$E(t) = \sum_{t'=t-\frac{w}{2}}^{t+\frac{w}{2}} a(t')^2 \tag{1}$$

where a is the amplitude of a sample and w is the length of the time window. For this study the average energy of the diffraction image is used to highlight structure that is resolved by the diffraction image. All examples in this study use a time window of 5 ms.

3.4 Constraining the Location of Out-of-plane Diffractors

For 2-D seismic profiles, so called out-of-plane reflections (i.e., reflections from outside the vertical plane of the profile) can contaminate the image. The illumination of seismic reflectors depends on the local dip of the reflector and the geometry of the receiver array. Diffractors, however, are fully illuminated from all angles even by single-channel, zero-offset data. This means that 2-D diffraction images suffer more strongly from out-of-plane diffraction energy than corresponding reflection images. In addition, mass-transport complexes are inherently 3-D geobodies, so 2-D seismic images of mass-transport complexes will, in general, suffer more strongly from out-of-plane energy than 2-D images of regular sedimentary geology. Therefore diffraction images of mass-transport complexes from 2-D seismic profiles are expected to contain particularly large amounts of energy contributed from outside the plane of the section.

The apparent TWTT of an out-of-plane point diffractor (t_{diffr}) can be predicted (Fig. 3) from the cross-line distance to the diffractor (x), the depth of the diffractor below the seismic datum (z) and the average velocity along the raypath from the seismic array to the diffractor (v_{rms}):

$$t_{diffr} = \frac{2\sqrt{x^2 + z^2}}{v_{rms}}. \tag{2}$$

Assuming that diffractors are evenly distributed throughout the mass-transport complex, some of the diffraction energy will always come from *outside* the vertical plane of the profile (i.e., $|x| > 0$ in Fig. 3). If the body is wider than it is thick, the apparent

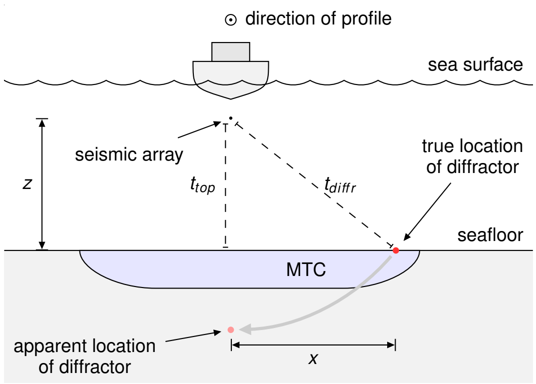

Figure 3. Cross-sectional view of marine seismic acquisition in the direction of the seismic profile, showing how an out-of-plane diffractor at the seafloor will appear to “swing” into the profile. The tow depth of the source and receiver arrays (seismic datum) is marked. z is the depth of the diffractor with respect to the seismic datum, x is the horizontal offset of the diffractor perpendicular to the profile. t_{top} and t_{diffr} are the two-way travel times to the top of the mass-transport complex (MTC) and the diffractor, respectively.

thickness of the slide from diffraction images will be greater than the apparent thickness of the slide from reflection images. This results in a “shadow” of diffraction energy below the true basal surface of the mass-transport complex in 2-D seismic data.

We can use this “diffraction shadow” to quantify the width, perpendicular to the profile, of the zone of potential diffractors that contribute to the image. For a mass-transport complex exposed at the seafloor we can make the simplifying assumption that potential internal diffractors are at, or near, the seafloor, so $v_{rms} \approx v_{water}$. We consider that the seafloor is equivalent to the potential top surface of the mass-transport complex. The seafloor depth is known independently from multi-beam swath bathymetry.

The workflow to calculate the zone of diffractors that contribute to the image is as follows:

1. Calculate the horizontal offset of each point on the seafloor from the profile (x).
2. Calculate the TWTT from the seismic profile (at datum) to the potential top surface of the body (seafloor depth) (z) using Eq. 2 with $v_{rms} \approx v_{water} = 1500\,\mathrm{ms}^{-1}$.
3. Pick the apparent base of the mass-transport complex (t_{diffr}) from the diffraction image, using the outline of the “diffraction shadow” associated with the body.

4. Project t_{diffr} perpendicular to the profile onto the TWTT contour calculated in (2).

The distance from the profile to the projected base of the "diffraction shadow" tells us the minimum extent of the zone of diffractors from the profile, in the direction of maximum extent. If we assume that the majority of diffraction energy is generated by the mass-transport complex, instead of by the un-failed sediments, this gives an approximation of the minimum extent of the slide perpendicular to the profile. It doesn't, however, tell us in which direction that extent could be. The method can be extended to buried bodies if subsurface velocity information is known. Whilst it is a crude technique, it may be useful to estimate the minimum width of mass-transport complexes that are intersected only by single, 2-D seismic profiles in the absence of other geophysical data.

4 Results

4.1 Diffraction Imaging

4.1.1 Profile INS2-Line1

The INS2-Line1 seismic profile largely consists of parallel, high-amplitude Plio-Quaternary reflectors, pierced by the Lolita salt diapir, forming a dome at the seafloor approximately 4 km wide in the centre of the profile (Fig. 4). The doming has resulted in slope failures that radiate from the centre of the dome, visible in the bathymetry (Fig. 1c). To the north the upper Late Quaternary sediments onlap and pinchout, which characterises a major contourite drift deposit resulting from bottom currents associated with the Mediterranean Outflow Water. Two prominent mass-transport complexes (MTC A and MTC B) are exposed at the seafloor on either side of the diapir and are clearly visible on the conventional seismic reflection image (Fig. 4a). MTC A has an in-profile length of approximately 7.4 km and a maximum in-profile thickness of approximately 75 ms TWTT. MTC B has an in-profile length of approximately 7.2 km and a maximum in-profile thickness of approximately 175 ms TWTT. MTC A originated from the drift deposits, whereas MTC B originated from the salt diapir. Both propagated towards the south.

Fig. 4b shows the unmigrated stack of INS2-Line1. Diffraction tails are visible originating from the rugose, high-amplitude seafloor and top salt interfaces. Fig. 4c shows the local dip estimate (de-migrated dip field estimated from the conventional seismic re-

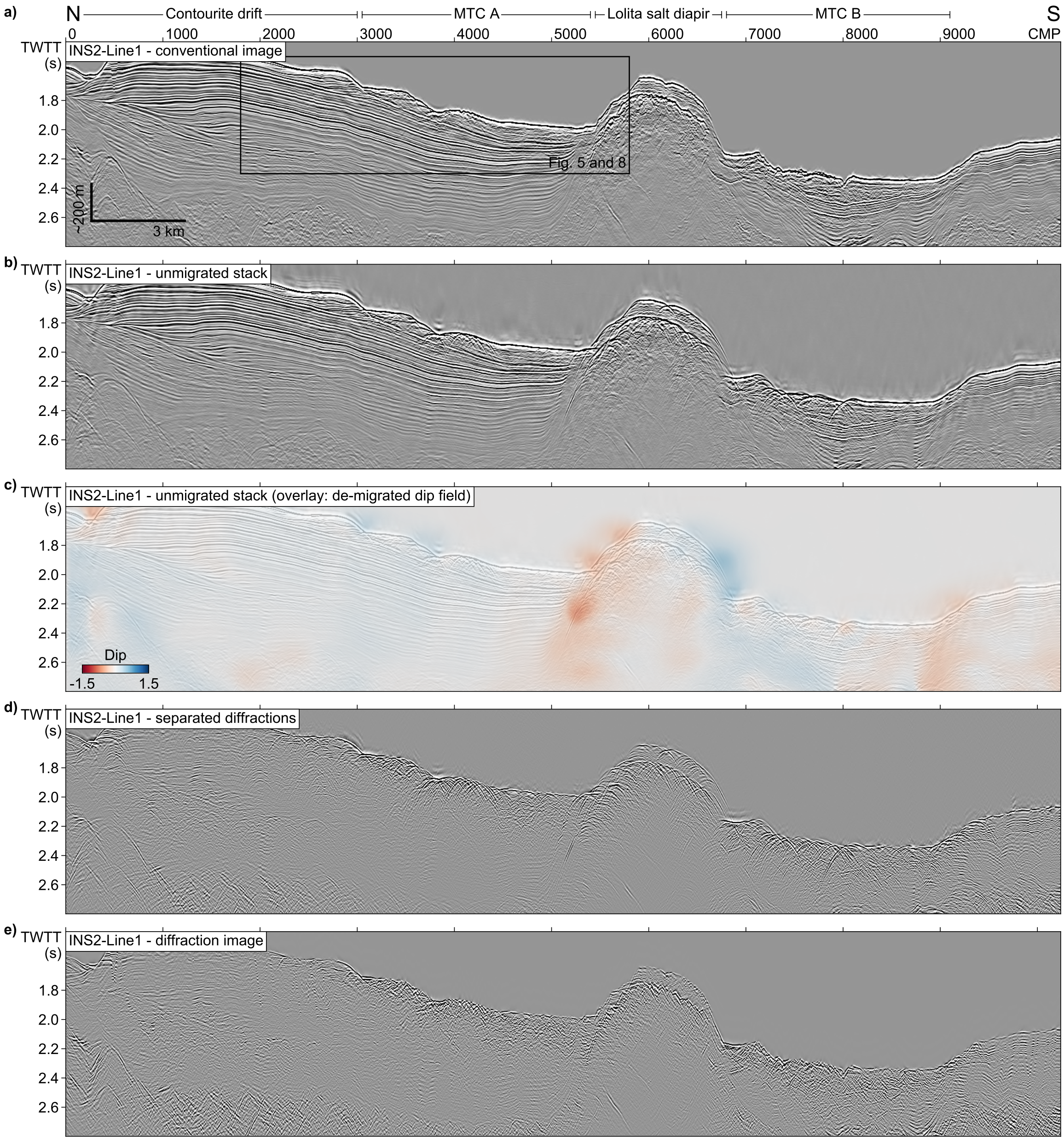

Figure 4. Seismic profile INS2-Line1 from the Portimão Bank area (Fig. 1). a) Conventional migrated seismic image. b) Unmigrated stacked conventional data (reflections and diffractions). c) De-migrated estimated dip field overlaid on the unmigrated conventional stack. d) Separated diffractions, stacked. e) Diffraction image.

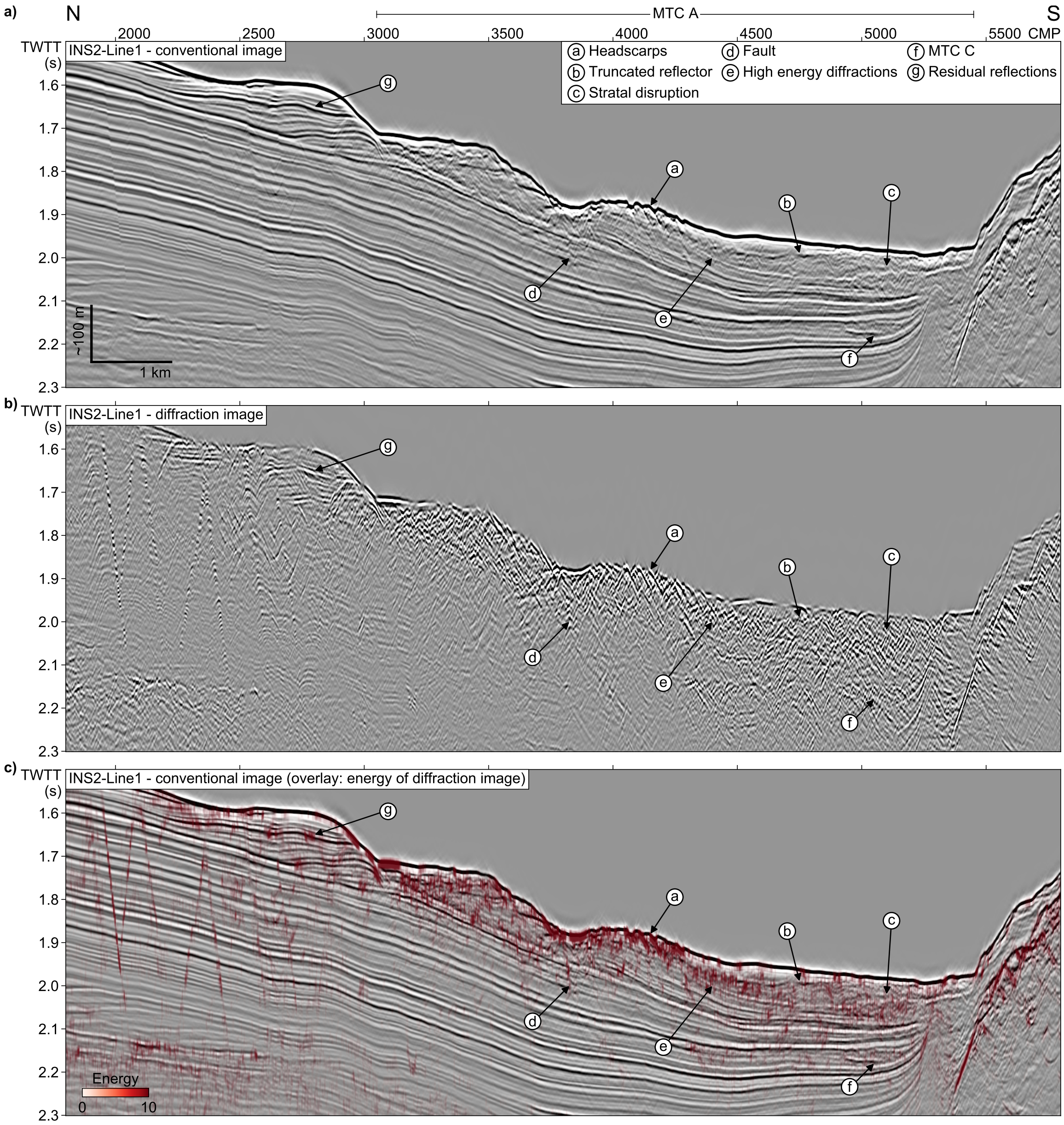

Figure 5. A section of seismic profile INS2-Line1 (Fig. 4) from the Portimão Bank area containing a prominent mass-transport complex. Interpreted structure is labelled. a) Conventional image, migrated reflections and diffractions. b) Diffraction image, migrated diffractions. c) Energy of diffraction image overlaid onto conventional image, to highlight location of diffractors.

flection image) overlaid on the unmigrated stack. The dip estimate appears to follow the dip of the prominent horizons well.

Fig. 4d shows a stack of the separated diffractions. This view is comparable to the unmigrated stack (Fig. 4b). Diffraction tails are clearly seen throughout the section, including from i) a series of normal faults (CMPs 1500 to 3000); ii) inside both prominent mass-transport complexes (CMPs 3000 to 5500 and 7000 to 9000) and iii) within the deeper, chaotic olistostrome unit (CMPs 1000 to 5000 and 9000 to 10 000, below around 2.4 s). Fig. 4e shows the diffraction image (the migrated separated diffractions). The diffraction image shows high amplitudes inside MTC A and MTC B, at the rugose top salt interface and inside the deeper olistostrome unit. Some residual reflection energy remains, particularly in areas of rapidly varying dip (see Fig. 5, label "g").

4.1.2 Profile MP06b

The MP06b seismic profile shows a cross-sectional view of the Marquês de Pombal fault, a monoclinal reverse fault (Fig. 6). The profile can be divided into two main sections: the Infante Don Henrique Basin (the footwall of the Marquês de Pombal fault, water depth around 3800 m) and the steeply dipping slope area (the frontal part of the hanging wall of the Marquês de Pombal fault, water depth around 2500 m at the south eastern edge of the profile). The conventional seismic reflection image (Figs. 6a and 7a) shows that the Infante Don Henrique Basin contains a stacked succession, >1 s TWTT thick, of mass-transport complexes, separated by parallel horizons representing the background hemipelagic deposition. The hanging wall of the Marquês de Pombal fault shows greater deformation – the shallow part of the slope shows extremely disordered, overlapping horizons that reflect the complex seafloor topography caused by mass-wasting in the slope area. The Marquês de Pombal fault plane is not directly imaged in this data; the fault zone is represented by an area of relatively low amplitude, disordered reflectors, dipping to the south east (CMPs 1900 to 2500, 5.25 s to 6.5 s TWTT).

Fig. 6b shows the unmigrated stack of MP06b. Diffraction tails are visible originating from the rugose seafloor in the steeply dipping hanging wall area (CDPs 1800 to 3000) and from truncated reflectors where the Infante Don Henrique Basin meets the low amplitude, disordered zone containing the Marquês de Pombal fault. Fig. 6c shows the local dip estimate (de-migrated dip field estimated from Fig. 6a) overlaid on the unmi-

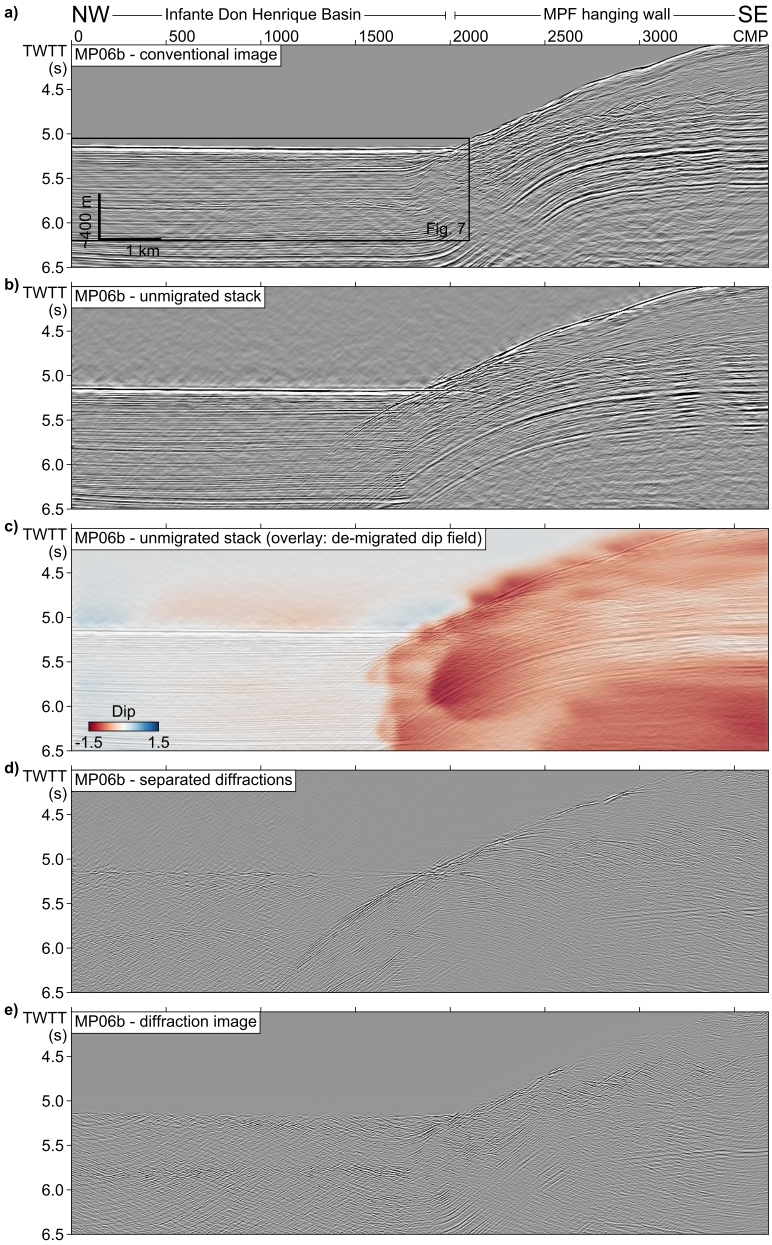

Figure 6. Seismic profile MP06b from the Marquês de Pombal fault zone area (Fig. 1). The Marquês de Pombal fault (MPF) is located around CMP 2000. a) Conventional migrated seismic image. b) Unmigrated stacked conventional data (reflections and diffractions). c) De-migrated estimated dip field overlaid on the unmigrated conventional stack. d) Separated diffractions, stacked. e) Diffraction image.

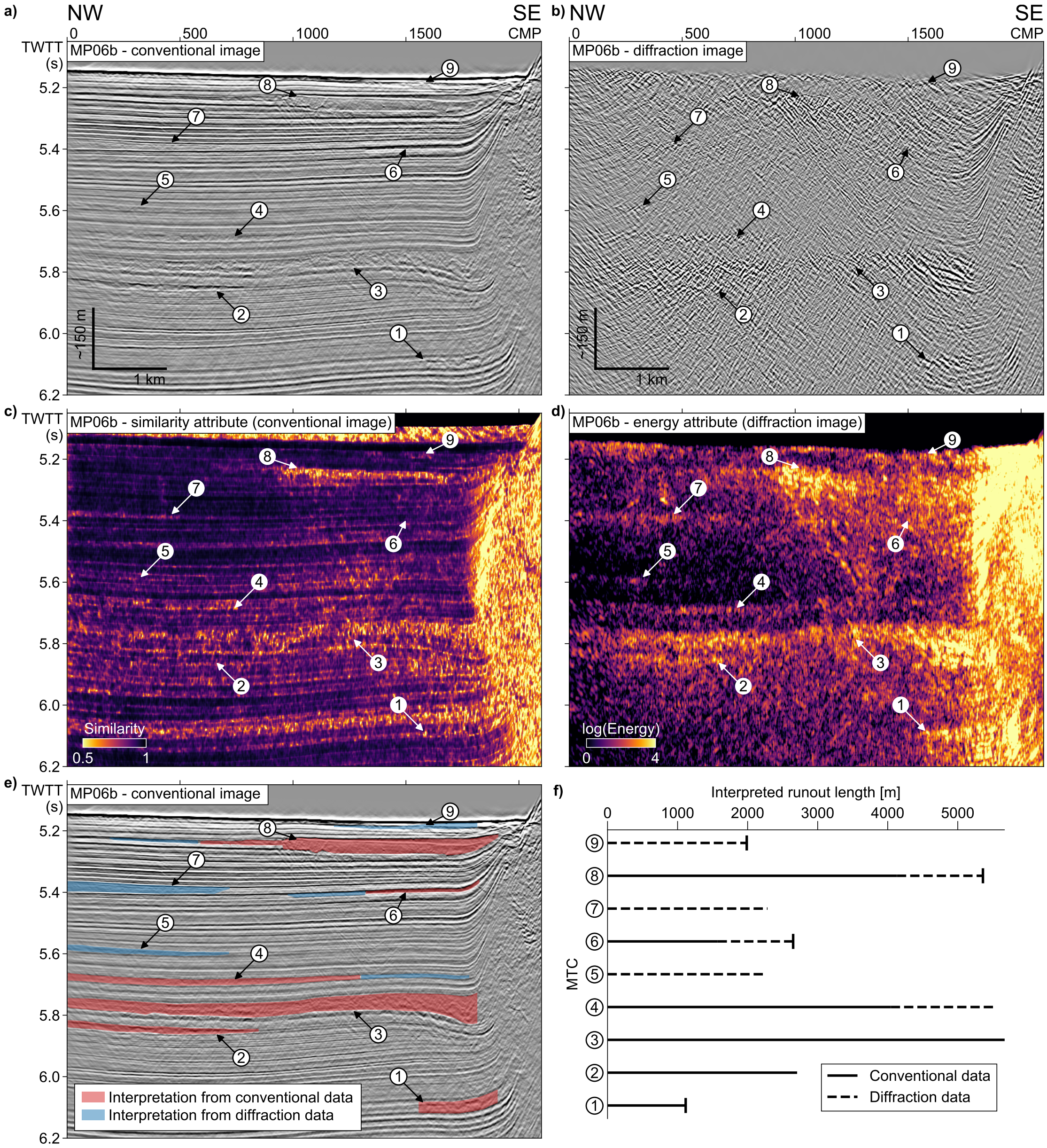

Figure 7. A section of seismic profile MP06b from the Marquês de Pombal fault area (Fig. 6). Interpreted mass-transport complexes are labelled from 1 to 9. Conventional imaging products: a) the conventional seismic reflection image and c) the similarity attribute of the conventional image. Diffraction imaging products: b) the corresponding diffraction image and d) the energy attribute of the diffraction image. e) The interpreted mass-transport complexes overlaid on the conventional image. The extent of the bodies interpretable from the conventional products is filled red, the extent interpretable from the diffraction products is filled blue. f) The proportion of the interpreted runout length of each body interpreted from the diffraction products versus the conventional products.

grated stack. In general, the dip estimate appears to follow the dip of the prominent horizons well, showing near-zero dip in the Infante Don Henrique Basin and negative dip (dipping to the north west) in the hanging wall area. The south eastern, deep corner of the profile (CMPs >2500, >5.5 s TWTT) shows anomalously high dips, corresponding to steeply dipping noise, due to low signal-to-noise ratio in this deeper area.

Fig. 6d shows a stack of the separated diffractions. This section is comparable to the unmigrated stack (Fig. 6b). Diffraction tails are clearly seen throughout the section, particularly from disrupted reflectors in the hanging wall area (CMPs 2000 to 4200) and corresponding to mass-transport complexes in the Infante Don Henrique Basin (CMPs 0 to 2000, 5.2–6 s TWTT). Fig. 6e shows the diffraction image (the separated diffractions after migration). The diffraction image shows laterally continuous, high-amplitude areas that correspond to mass-transport complexes seen in the conventional image. Some residual reflection energy remains, particularly in the area of rapidly varying dip at the break in slope corresponding to the Marquês de Pombal fault (CDP 2000).

4.2 Comparison of Reflection and Diffraction Images of Internal Struture

Fig. 5 shows a section of seismic profile INS2-Line1 around MTC A, a mass-transport complex exposed at the seafloor (Fig. 4). It shows the conventional seismic reflection image (Fig. 5a), the corresponding diffraction image (Fig. 5b) and the energy of the diffraction image overlaid on the conventional image (Fig. 5c). Diffraction energy is concentrated inside MTC A compared to the un-failed underlying sediments. We interpret the high-amplitude diffractions as resulting from: (a) headscarp faults in an extensional part of the mass-transport complex; (b) a truncated internal reflector within the mass-transport complex; (c) a zone of intense stratal disruption within the mass-transport complex (possibly the interface between two separate mass-transport deposits); (d) a small normal fault directly beneath the mass-transport complex, likely related to sediment loading/unloading after failure; (e) a zone of diffuse, high energy diffractions that is not clearly related to structure resolved by the reflection image and (f) a smaller, deeper mass-transport complex (MTC C). The remaining diffraction energy within the mass-transport complex has complex geometry and is not clearly related to structure resolved by the reflection image (e.g., the area labelled “e”).

4.3 Comparison of Diffraction Image with Similarity Attribute

Fig. 7 shows a section of seismic profile MP06b, focused on the stacked succession of mass-transport complexes in the Infante Don Henrique Basin. Fig. 7a shows the conventional seismic reflection image and Fig. 7c shows the similarity attribute of the conventional image (hereafter referred to as “conventional products”). Fig. 7b shows the diffraction image and Fig. 7d shows the logarithm of the energy attribute of the diffraction image (hereafter referred to as “diffraction products”).

Nine mass-transport complexes are interpreted from a combination of the conventional and diffraction products (labelled in order of decreasing depth from 1 to 9). Interpretation of a mass-transport complex is guided by one or more of the following features: i) apparently chaotic or transparent seismic character in the conventional reflection image; ii) bounded by high-amplitude, laterally continuous top and/or basal reflectors; iii) lobe shaped, laterally consistent low similarity values or iv) lobe shaped, laterally consistent high-amplitude diffraction energy. Some large bodies are visible directly from the conventional reflection image (e.g., MTC3 and MTC8). Other bodies are only clearly resolved by the diffraction image (e.g., MTC5 and MTC7).

Fig. 7e shows the interpreted lateral extent and thickness of the interpreted bodies overlaid on the conventional image. The portion of the bodies interpreted from the conventional products versus the diffraction products is indicated. Fig. 7f shows the interpreted total length (runout) of these bodies, indicating the proportion of the total length that was interpretable only from the diffraction products. Several of the bodies runout past the end of the section, so the interpreted runout length is a lower bound on their total length. MTC4 and MTC6 are both resolved from the conventional products, but their runout length is extended by >1.5 km and 1.1 km respectively using the diffraction products. MTC7 is only clearly resolved by the diffraction image, likely because it has an apparently transparent seismic character in the conventional image, whereas the diffraction image clearly resolves a lobe shaped zone of heterogeneity. MTC9 is a 2 km long body near the seafloor which is only visible in the diffraction image, likely because it is thinner than the high-amplitude seismic reflectors in the conventional image.

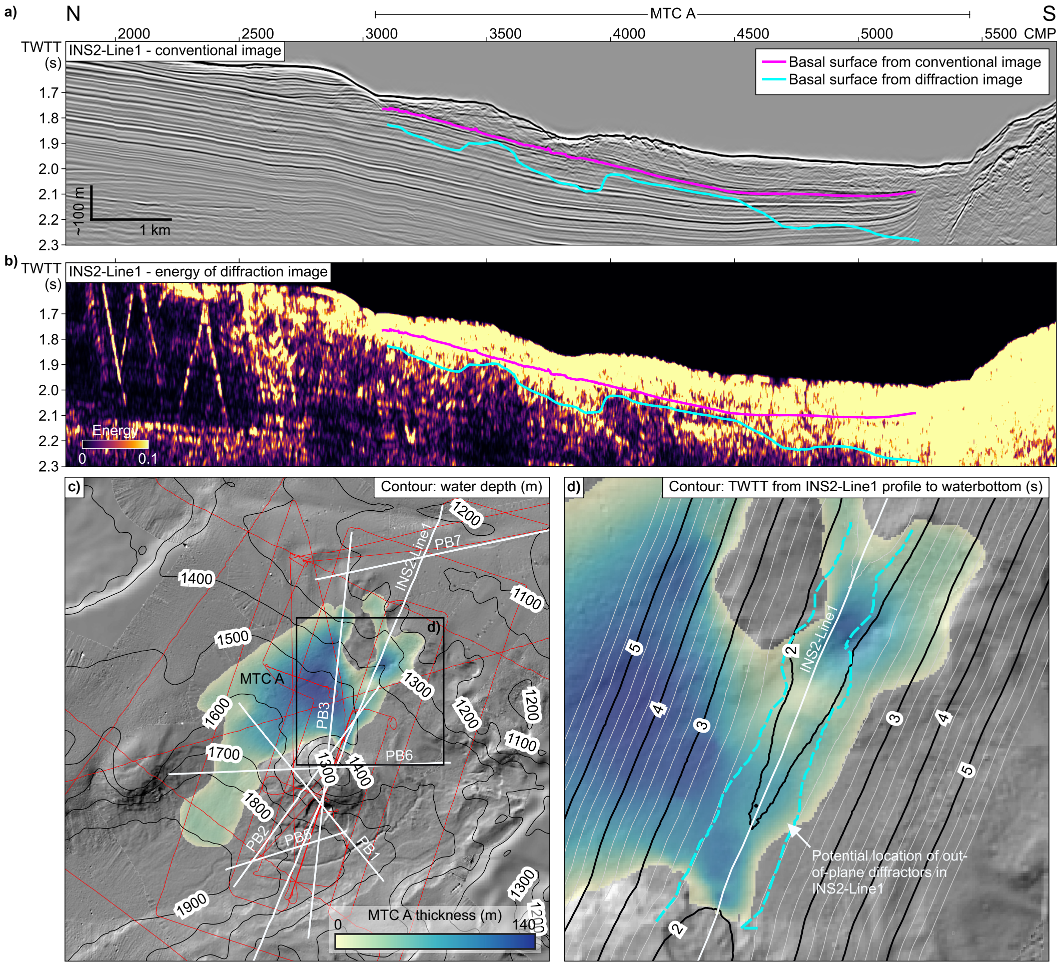

Figure 8. A section of seismic profile INS2-Line1 (Fig. 4) from the Portimão Bank area containing a prominent mass-transport complex, MTC A. a) The conventional seismic image. b) The energy of the diffraction image. The pink horizon is the interpreted basal surface of MTC A from the conventional image, the blue horizon is the interpreted base of the out-of-plane diffraction energy associated with MTC A, the "diffraction shadow". c) The water depth (contours) on the shaded relief of the area surrounding the Lolita salt diapir. The extent and thickness of MTC A is interpreted from the bathymetry, sub-bottom profiler data (red) and a network of multi-channel seismic profiles (white). d) The two-way travel time (TWTT) contour from INS2-Line profile seismic datum to the potential top MTC A surface (seafloor) (maximum record length is 5.8 s). The dashed blue line indicates the zone of potential locations for the out-of-plane diffractors, projected both directions perpendicular from the line.

4.4 Extent of Mass-Transport Complex Perpendicular to Profile

Fig. 8a and Fig. 8b show the true basal surface of MTC A picked from the conventional seismic reflection image (INS2-Line1), alongside the picked base of the "diffraction shadow" associated with MTC A. Fig. 8c shows the lateral extent and thickness of MTC A, interpreted from a combination of multi-channel seismic and sub-bottom profiler lines and the bathymetry, giving a total volume of $5.5\,\mathrm{km}^3$ (converted from time to depth using the sediment velocity gradient of $200\,\mathrm{ms}^{-2}$). Fig. 8d shows the TWTT contour to the potential top surface of MTC A (the seafloor) from seismic profile INS2-Line1 (calculated using Eq. 2), with the TWTT of the base "diffraction shadow" projected onto the contours (blue dashed line). This zone shows the limit, perpendicular to the profile, of the potential locations of diffractors which contribute to the diffraction shadow associated with MTC A. These diffractors could include embedded blocks, rough topography from the basal surface of the mass-transport complex and other heterogeneous structure.

5 Discussion

5.1 Imaging Internal Structure

The results of diffraction imaging applied to MTC A (INS2-Line1) are shown in Fig. 5. The diffraction image clearly images a zone of normal faults between CMPs 1800 to 3000 and the rugose top salt interface of the Lolita salt diapir. There is a significantly higher concentration of diffraction energy within MTC A compared to the surrounding un-failed sediments. This suggests that the internal structure of MTC A is significantly more heterogeneous than the un-failed sediments, which can already be seen from the conventional seismic image. This is consistent with outcrop examples of mass-transport complexes, which show that complex internal structure can be preserved (Lucente & Pini, 2003). We observe high-amplitude diffractors that coincide with structure observed on the reflection image related to MTC A: headscarp faults, truncated internal interfaces and strong stratal disruption. This is the type of small-scale geological heterogeneity that we would expect to generate diffractions.

Diffractors that do not coincide with structure seen in the conventional image are also resolved (labelled "e" in Fig. 5). In the absence of high-resolution data, such as cores or sub-bottom profiler images, it is not clear exactly what structure this could represent, but we speculate that this may be related to fine-scale internal structure, such as local shear zones, intact embedded blocks or fluid escape features, which is below the resolution of the conventional image. Diffractions require both lateral heterogeneity (around or below the scale of the seismic wavelength) *and* an impedance contrast (Bachrach & Reshef, 2010), so the presence of a zone of consistent high-amplitude diffractions within a body is evidence that significant metre- to decametre-scale heterogeneity (internal structure) is preserved after transport and emplacement. Diffraction images can thus provide information on the degree of internal disaggregation, by quantifying the degree of geological heterogeneity at scales close to the seismic resolution. This could provide an extra source of information to constrain flow type, for example to differentiate between debris flows (complete disaggregation), slumps (pre-failure internal interfaces deformed but largely preserved) and the transition between both end members. The high-amplitude diffraction image response observed in Fig. 5b supports an interpretation of MTC A as a "structured" rather than "structureless" deposit, even if the morphology of such structure is not well-resolved by seismic methods.

We also clearly resolve a normal fault plane *below* MTC A in the diffraction image (labelled "d" in Fig. 5). This is associated with an approximately 500 m wide, channel-shaped depression on the top surface of MTC A around CMP 3750. We interpret this to be the result of sediment loading due to the emplacement of MTC A on the previously competent sediments, as the fault becomes blind at depth. As well as resolving structure within mass-transport complexes, diffraction imaging is able to image fine-scale structure in the un-failed sediments immediately *below* the body.

5.2 Discrimination of Events Near the Limit of Seismic Resolution

Fig. 7 shows the results of diffraction imaging applied to part of seismic profile MP06b. In this profile, the Infante Don Henrique basin shows a >1 s TWTT thick succession of stacked mass-transport complexes. Some large events ($n = 6$) are clearly visible on the conventional seismic image as apparently chaotic bodies with well-defined top and basal reflectors. The diffraction image, however, reveals several smaller events ($n = 3$) that are difficult to identify or are ambiguous in the conventional image and associated discontinuity attribute. These include i) a thin event (average thickness approximately 18 ms TWTT) that is not seen in the conventional image (MTC5); ii) a thin event (average thickness approximately 14 ms TWTT), close to the waterbottom, obscured by high-amplitude shallow reflections in the conventional image (MTC9) and iii) two events that appear as a single event in the conventional image, but are clearly resolved as two separate events in the diffraction image (MTC6 and MTC7). In addition, the diffraction imaging products allow better definition of the lateral extent (runout) of bodies. We are able to follow the runout of some events for significant extra distance (on the order of kilometres for seismic profile MP06b) compared to the conventional seismic image (Fig. 7f). The diffraction image, and corresponding energy attribute, clearly highlights these events.

We also observe this effect on seismic profile INS2-Line1 (Fig. 5). Here, there is a small mass-transport complex (MTC C, labelled "f" in Fig. 5) below the larger event, MTC A. From the conventional image MTC C is represented by a high-amplitude basal horizon that extends for about half of the total length of the body. The diffraction image clearly shows a lobe shaped zone of heterogeneity, approximately 500 m in length, that we interpret as a small mass-transport complex that failed towards the north, originating from the dome associated with the Lolita salt diapir.

Diffraction images offer higher lateral (horizontal) resolution because they overcome the lateral resolution limit of reflection images. They offer potentially higher temporal (vertical) resolution because relatively high-amplitude and thick specular reflections, which can obscure events that are thinner than the dominant seismic wavelength, are eliminated during the diffraction separation. In the context of screening for mass-transport complexes, diffraction images clearly improve the discrimination of relatively small, thin events (on the order of 10 ms thick) and allow more accurate delineation of their total lateral extent, when a significant proportion of the body is thinner than the reflection image can resolve. This is particularly important to characterise the flow properties of such events from seismic data. For example, many events have a substantial component of fine sediment that runs out a significant distance beyond the main cohesive body of the event, pinching out at zero thickness at the true maximum extent of the flow. This type of thin deposit, parallel to the background sedimentation, is difficult to image with conventional seismic reflection images.

The record of buried mass-transport complexes identified from marine geophysical data is biased toward events that can be clearly resolved in multi-channel seismic reflection images (i.e., relatively thick and laterally extensive). This means that catalogues of mass-transport complexes are biased towards larger events, or younger events that are still preserved in the bathymetry (e.g., Urgeles & Camerlenghi, 2013). Screening for mass-transport complexes using diffraction imaging will allow for a more complete catalogue of smaller, deeper events.

5.3 Comparison to Seismic Discontinuity Attributes

Similarity and other discontinuity attributes are routinely computed as part of a traditional geohazard interpretation workflow in order to characterise, delineate and screen for mass-transport complexes (e.g., Alves et al., 2014; Bhatnagar et al., 2019). Here we calculate the similarity attribute of the conventional seismic reflection image to compare to the energy attribute of the diffraction image (Fig. 7). There are high-level similarities between the two: relatively large events (MTC3, MTC4 and MTC8) are clearly imaged by both methods. Many smaller events, however, are not clearly delineated from the background geology by the similarity attribute. Moreover, the similarity attribute seems to be sensitive to features other than geological heterogeneity — we see noise from high-amplitude laterally continuous horizons at a similar amplitude to the genuinely disordered geology of the mass-transport complexes. It is difficult to discriminate a high-amplitude, horizontal un-failed horizon from a thin mass-transport complex using the similarity attribute.

We argue that when screening for mass-transport complexes, diffraction images and derived attributes may be more useful than discontinuity attributes of reflection images, because they are more sensitive to the target (i.e., heterogeneous geology) and they contain lower "noise" generated by high-amplitude, coherent reflections. The diffraction image suffers less from interference from high-amplitude reflections, or edge effects and smoothing that may be introduced by window-based attributes. Diffraction images and derived attributes are a more "physically correct" alternative to conventional attributes because diffraction images directly image subsurface heterogeneity (i.e., fine scale disordered geology) at the scale of the seismic wavelength or below.

5.4 Constraining the Lateral Extent of Mass-transport Complexes From 2-D Profiles

In Section 3.4 we propose a simple method to constrain the location of out-of-plane diffraction energy imaged by 2-D seismic profiles. The results can be used to put a minimum bound on the lateral extent (perpendicular to the profile) of the zone of diffractors associated with a strongly heterogeneous body. In other words, it offers a constraint on the minimum width of a mass-transport complex imaged by a 2-D seismic profile.

We demonstrate the method by applying it to INS2-Line1, where there is a well defined "diffraction shadow" beneath MTC A (Fig. 8b). The presence of such diffractions beneath the apparent basal surface, but clearly associated with the heterogeneous body, indicates that the diffraction image contains contributions from outside the plane of the profile. The results of the method give a minimum bound on the width of the zone of out-of-plane diffractors that contribute to the diffraction image. This can give an estimate of the minimum width of a body that contains many diffractors (i.e., a mass-transport complex) from a 2-D seismic profile. It doesn't constrain the direction of the diffractors relative to the profile, or what the *maximum* width of the diffractor zone could be. It depends on being able to estimate the top surface of the body (which could be assumed to be approximately horizontal, for most mass-transport complexes) and assumes that the body is thin compared to the water depth. It also relies on being able to separate diffractions generated by the body (the "diffraction shadow") from diffractions generated by the background geology surrounding the body, which may not always be straightforward.

The method is simple but nevertheless could be a useful way to estimate a lower bound on the extent of mass-transport complexes from a single 2-D seismic profile, where other geophysical information is not available. This is a common scenario when screening for mass-transport complexes for marine geohazard studies in frontier areas; for academic and vintage datasets; and in polar areas, where acquiring 3-D towed-streamer seismic data may be impossible due to year-round ice cover. It is trivial to extend the method to deal with buried mass-transport complexes, so long as i) the velocity model to the top of the body is known; ii) the slide is thin relative to its depth; and iii) the topography of the top surface is small, relative to its depth.

5.5 Limitations of Diffraction Imaging to Characterise Mass-transport Complexes

Whilst we have shown that diffraction images clearly offer better imaging of heterogeneous geology compared to reflection images, there remain some limitations, particularly regarding the data used for this study and the specific application to characterise mass-transport complexes.

5.5.1 Incomplete Diffraction Separation

Diffraction imaging relies on good separation between the diffracted and reflected wavefields. Here, we perform the diffraction separation in common-offset domain using PWD filters to eliminate laterally continuous reflections (Section 3.2.2). Subaqueous mass-failures tend to occur in environments that are geologically complex such as canyons, tectonically active areas and diapiric areas. This means that seismic images in such environments are also likely to contain strong variation in dip, reflections that are not laterally continuous and high-amplitude reflections and diffraction tails generated by a rugose seafloor. These factors can prevent reliable estimation of the true dip field from unmigrated seismic profiles. Our solution is to estimate the dip field on migrated data, and de-migrate the dip field for diffraction separation on the unmigrated common-offset sections (Section 3.2.1). In general, the results of the dip estimation and de-migration are adequate for diffraction separation to image the shallow mass-transport complexes in this study. There are, however, some residual reflections that are not eliminated during diffraction separation, for example due to the conflicting dips within the contourite drift (Fig. 5, labelled “g”) and at the break of slope across the Marquês de Pombal fault (Fig. 7, around CMP 1800). These become “noise” in the diffraction images. Fortunately, residual reflections are straightforward to identify in the diffraction image, because they appear at the same location as in the conventional image.

There are other diffraction separation methods that potentially may be more effective for imaging mass-transport complexes. These include post-migration diffraction separation in dip-angle domain (Reshef & Landa, 2009) and diffraction separation by adaptive subtraction of the coherent reflected wavefield (Schwarz, 2019). The choice of method strongly depends on the type of seismic acquisition (e.g., streamer length compared to target depth, lateral and vertical image resolution, 2-D vs 3-D acquisition geometry) and data characteristics (e.g., amplitude of diffractions relative to reflections, noise level). In all cases care should be taken during the pre-processing flow to preserve diffraction energy.

5.5.2 Diffraction Imaging of 2-D Seismic Profiles

In this study we apply diffraction imaging to 2-D multi-channel seismic profiles. Seismic imaging in 2-D assumes that recorded energy is reflected or diffracted from a 2-D vertical plane. This may be a reasonable assumption where geological structure is 1-D perpendicular to the plane of the profile (a so-called *dip line*). When reflectors dip obliquely with respect to the profile, reflections cannot be properly imaged with a 2-D migration. Energy reflected from out-of-plane becomes "noise" or may interfere with primary in-plane energy. Mass-transport complexes are inherently three-dimensional geobodies. In addition to internal structure, they often show rugose, non-conformal upper and basal surfaces that can generate high-amplitude reflections and diffractions. This means that there is rarely an optimal "dip direction" to acquire a well-imaged 2-D seismic profile to image the internal structure of a mass-transport complex. In other words, out-of-plane energy is a common feature of seismic images of mass-transport complexes, and the situation with out-of-plane diffractions is worse than for reflections.

For diffraction imaging the consequences of this out-of-plane energy include misplaced out-of-plane diffractions (sometimes resulting in a "diffraction shadow" below mass-transport complexes; Section 3.4) and diffraction tails that are not properly collapsed by migration. This impedes migration velocity analysis methods which rely on focusing diffraction tails (e.g., Fomel et al., 2007; Decker et al., 2017). For this study velocity analysis was not possible due to the large proportion of out-of-plane diffractions in the shallow part of the section.

We suggest that mass-transport complexes contribute a significant amount of diffraction energy that is likely misplaced on 2-D seismic profiles, even in conventional seismic images. We hypothesise that this out-of-plane energy contributes to the apparently "chaotic" seismic texture commonly seen in mass-transport complexes. This underlines the importance of using 3-D seismic data for good imaging and proper reconstruction of the geometry of the internal structure of mass-transport complexes, for both conventional seismic reflection imaging and diffraction imaging.

6 Conclusions

In this study we use two 2-D multi-channel seismic profiles from the Gulf of Cadiz, south west Iberian Margin to compare the ability of diffraction imaging with conventional seismic reflection imaging to characterise mass-transport complexes. We find that mass-transport complexes generate a relatively large contribution of diffracted energy compared to the surrounding un-failed sediments, likely due to their heterogeneous internal structure and rugose erosional basal surface. Diffraction images can be considered to primarily image heterogeneous, small-scale geological structure and have higher lateral resolution in comparison to conventional reflection images. By overlaying the diffraction images on the conventional images we show that the diffraction images can resolve internal structure within such bodies. We speculate that the remaining diffraction energy is related to small-scale structure that is below the resolution of the reflection image.

Our results suggest that diffraction imaging can be:

1. used to quantify the degree of heterogeneity within a body, important for assessing the degree of disaggregation from transport and emplacement.
2. considered as a more physically correct alternative to traditional seismic discontinuity attributes, because it directly images subsurface heterogeneity.
3. used as an alternative to seismic discontinuity attributes to better delineate relatively small or thin bodies that are close to the resolution of the conventional seismic image.
4. used to estimate the minimum extent of mass-transport complexes in a direction perpendicular to a 2-D seismic profile.

Our results underline the importance of using 3-D seismic data to image mass-transport complexes, and the importance of preserving diffractions through the processing flow. Characterisation of mass-transport complexes and their internal structure is a promising new application of diffraction imaging, potentially bridging the “resolution gap” between seismic and outcrop data.

Appendix A Dip De-migration

The aim of dip de-migration is to recover the unmigrated dip field from a dip field estimated on a migrated image. We use this technique due to the presence of high-amplitude, steeply dipping diffraction tails and poor reflector continuity throughout the unmigrated data used in this study.

We perform the dip de-migration using simple geometric relations that describe how migration affects dipping reflectors in 2-D (Yilmaz, 2001):

1. The local dip in a migrated section is greater than in the unmigrated section (migration *steepens* reflectors).
2. For areas of non-zero local dip the horizontal distance between points is shorter after migration.
3. Migration moves events in an up-dip direction.

After Chun and Jacewitz (1981), for migrated dip α', unmigrated dip α, local migration velocity, v, and TWTT t:

$$\begin{aligned} \alpha' &= \frac{\alpha}{\sqrt{1-(\frac{\alpha v(x,t)}{2})^2}} \\ x' &= \frac{v(x,t)^2 t}{4}\alpha \\ t' &= t\left(1-\sqrt{1-\frac{\alpha v(x,t)}{2}}\right). \end{aligned} \tag{A1}$$

We first solve for the un-migrated local dip value, $\alpha(x', t')$. Then we calculate the horizontal and vertical (time) shift ($x'-x$ and $t'-t$). The de-migrated dip field $\alpha(x,t)$ is estimated by applying image warping (with the horizontal and vertical shifts) to $\alpha(x', t')$. The effect is to reverse the effect of migration on the dip field, to "de-migrate" the dip field.

Acknowledgments

Code to reproduce the results in this study using Madagascar (Fomel et al., 2013) is included in the Supporting Information. Pre-stack seismic data used for this study will be archived with Zenodo (or another FAIR compliant repository) prior to acceptance.

The authors wish to thank the crew, technicians and scientific party of the INSIGHT cruises (Legs 1 and 2), particularly the onboard seismic processing team: R. Bartolomé, P. Brito, A. Calahorrano and E. Piazza. Data for this study was collected in the framework of the project INSIGHT (CTM2015-70155-R) funded by the Spanish "Ministerio de Ciencia e Innovación" and the European Regional Development Fund. J. Ford was supported by a Marie Curie Doctoral Fellowship through the SLATE Innovative Training Network within the European Union Framework Programme for Research and Innovation Horizon 2020 under Grant Agreement No. 721403.

References

Alves, T. M., Kurtev, K., Moore, G. F., & Strasser, M. (2014). Assessing the internal character, reservoir potential, and seal competence of mass-transport deposits using seismic texture: A geophysical and petrophysical approach. *AAPG Bulletin*, *98*(4), 793–824. doi: 10.1306/09121313117

Alves, T. M., & Lourenço, S. D. (2010). Geomorphologic features related to gravitational collapse: Submarine landsliding to lateral spreading on a Late Miocene–Quaternary slope (SE Crete, eastern Mediterranean). *Geomorphology*, *123*(1-2), 13–33. doi: 10.1016/j.geomorph.2010.04.030

Bachrach, R., & Reshef, M. (2010). 3D ultra shallow seismic imaging of buried pipe using dense receiver array: Practical and theoretical considerations. *GEOPHYSICS*, *75*(6), G45–G51. doi: 10.1190/1.3506560

Baptista, M., Heitor, S., Miranda, J., Miranda, P., & Victor, L. (1998). The 1755 Lisbon tsunami; evaluation of the tsunami parameters. *Journal of Geodynamics*, *25*(1-2), 143–157. doi: 10.1016/S0264-3707(97)00019-7

Baptista, M. A., & Miranda, J. M. (2009). Revision of the Portuguese catalog of tsunamis. *Natural Hazards and Earth System Sciences*, *9*(1), 25–42. doi: 10.5194/nhess-9-25-2009

Bhatnagar, P., Verma, S., & Bianco, R. (2019). Characterization of mass transport deposits using seismic attributes: Upper Leonard Formation, Permian Basin. *Interpretation*, *7*(4), SK19–SK32. doi: 10.1190/INT-2019-0036.1

Born, M., & Wolf, E. (1959). *Principles of optics: Electromagnetic theory of propagation, interference, and diffraction of light.* London Pergamon Press.

Brackenridge, R. E., Hernández-Molina, F. J., Stow, D. A. V., & Llave, E. (2013). A Pliocene mixed contourite–turbidite system offshore the Algarve Margin, Gulf of Cadiz: Seismic response, margin evolution and reservoir implications. *Marine and Petroleum Geology*, *46*, 36–50. doi: 10.1016/j.marpetgeo.2013.05.015

Bull, S., Cartwright, J., & Huuse, M. (2009). A review of kinematic indicators from mass-transport complexes using 3D seismic data. *Marine and Petroleum Geology*, *26*(7), 1132–1151. doi: 10.1016/j.marpetgeo.2008.09.011

Cardona, S., Wood, L. J., Day-Stirrat, R. J., & Moscardelli, L. (2016). Fabric Development and Pore-Throat Reduction in a Mass-Transport Deposit in the Jubilee Gas Field, Eastern Gulf of Mexico: Consequences for the Sealing Capacity of MTDs. In G. Lamarche et al. (Eds.), *Submarine Mass Movements and their Consequences: 7th International Symposium* (pp. 27–37). Springer International Publishing. doi: 10.1007/978-3-319-20979-1_3

Carter, L., Gavey, R., Talling, P., & Liu, J. (2014). Insights into Submarine Geohazards from Breaks in Subsea Telecommunication Cables. *Oceanography*, *27*(2), 58–67. doi: 10.5670/oceanog.2014.40

Chen, J., & Schuster, G. T. (1999). Resolution limits of migrated images. *GEOPHYSICS*, *64*(4), 1046–1053. doi: 10.1190/1.1444612

Chopra, S., & Marfurt, K. J. (2007). *Seismic Attributes for Prospect Identification and Reservoir Characterization*. SEG Books.

Chun, J. H., & Jacewitz, C. A. (1981). Fundamentals of frequency domain migration. *GEOPHYSICS*, *46*(5), 717–733. doi: 10.1190/1.1441211

Claerbout, J. F. (1992). *Earth Soundings Analysis: Processing Versus Inversion.* Blackwell Scientific Publications.

De Blasio, F. V., Issler, D., Elverhøi, A., Harbitz, C. B., Ilstad, T., Bryn, P., … Løvholt, F. (2003). Dynamics, Velocity and Run-Out of the Giant Storegga Slide. In J. Locat, J. Mienert, & L. Boisvert (Eds.), *Submarine Mass Movements and Their Consequences* (Vol. 19, pp. 223–230). Dordrecht: Springer Netherlands. (Series Title: Advances in Natural and Technological Hazards Research) doi: 10.1007/978-94-010-0093-2_25

Decker, L., Merzlikin, D., & Fomel, S. (2017). Diffraction imaging and time-migration velocity analysis using oriented velocity continuation. *GEOPHYSICS*, *82*(2). doi: 10.1190/geo2016-0141.1

Diviacco, P., Rebesco, M., & Camerlenghi, A. (2006). Late Pliocene Mega Debris Flow Deposit and Related Fluid Escapes Identified on the Antarctic Peninsula Continental Margin by Seismic Reflection Data Analysis. *Marine Geophysical Researches*, *27*(2), 109–128. doi: 10.1007/s11001-005-3136-8

Fomel, S. (2002). Applications of plane-wave destruction filters. *GEOPHYSICS*, *67*(6), 1946–1960. doi: 10.1190/1.1527095

Fomel, S., Landa, E., & Taner, M. (2007). Poststack velocity analysis by separation and imaging of seismic diffractions. *GEOPHYSICS*, *72*(6). doi: 10.1190/1.2781533

Fomel, S., Sava, P., Vlad, I., Liu, Y., & Bashkardin, V. (2013). Madagascar: open-source software project for multidimensional data analysis and reproducible computational experiments. *Journal of Open Research Software*, *1*(1), e8. doi: 10.5334/jors.ag

Gràcia, E., Vizcaino, A., Escutia, C., Asioli, A., Rodés, A., Pallàs, R., ... Goldfinger, C. (2010). Holocene earthquake record offshore Portugal (SW Iberia): testing turbidite paleoseismology in a slow-convergence margin. *Quaternary Science Reviews*, *29*(9-10), 1156–1172. doi: 10.1016/j.quascirev.2010.01.010

Gràcia, E., Dañobeitia, J., Vergés, J., Bartolomé, R., & Córdoba, D. (2003). Crustal architecture and tectonic evolution of the Gulf of Cadiz (SW Iberian margin) at the convergence of the Eurasian and African plates. *Tectonics*, *22*(4). doi: 10.1029/2001TC901045

Gràcia, E., Dañobeitia, J., Vergés, J., & Team, P. (2003). Mapping active faults offshore Portugal (36N–38N): Implications for seismic hazard assessment along the southwest Iberian margin. *Geology*, *31*(1), 83. doi: 10.1130/0091-7613(2003)031⟨0083:MAFOPN⟩2.0.CO;2

Gràcia, E., Urgeles, R., Rothenbeck, M., Wenzlaff, E., Steinführer, A., Kurbjuhn, T., ... INSIGHT Leg 1 cruise party (2018). *ImagiNg large SeismogenIc and tsunamiGenic structures of the Gulf of Cadiz with ultra-High resolution Technologies (INSIGHT) Leg 1 survey cruise report* (Tech. Rep.). Institut de Ciències del Mar - CSIC.

Khaidukov, V., Landa, E., & Moser, T. (2004). Diffraction imaging by focusing-defocusing: An outlook on seismic superresolution. *GEOPHYSICS*, *69*(6), 1478–1490. doi: 10.1190/1.1836821

Leynaud, D., Mulder, T., Hanquiez, V., Gonthier, E., & Régert, A. (2017). Sediment failure types, preconditions and triggering factors in the Gulf of Cadiz. *Landslides*, *14*(1), 233–248. doi: 10.1007/s10346-015-0674-2

Lo Iacono, C., Gràcia, E., Zaniboni, F., Pagnoni, G., Tinti, S., Bartolome, R., ... Zitellini, N. (2012). Large, deepwater slope failures: Implications for landslide-generated tsunamis. *Geology*, *40*(10), 931–934. doi: 10.1130/G33446.1

Lucente, C. C., & Pini, G. A. (2003). Anatomy and emplacement mechanism of a large submarine slide within a Miocene foredeep in the northern Apennines, Italy: A field perspective. *American Journal of Science*, *303*(7), 565–602. doi: 10.2475/ajs.303.7.565

Lumley, D. E., Claerbout, J. F., & Bevc, D. (1994). Anti-aliased Kirchhoff 3-D migration. In *SEG Technical Program Expanded Abstracts 1994* (pp. 1282–1285). Society of Exploration Geophysicists. doi: 10.1190/1.1822760

Løvholt, F., Bondevik, S., Laberg, J. S., Kim, J., & Boylan, N. (2017). Some giant submarine landslides do not produce large tsunamis. *Geophysical Research Letters*, *44*(16), 8463–8472. doi: 10.1002/2017GL074062

Matias, L. M., Cunha, T., Annunziato, A., Baptista, M. A., & Carrilho, F. (2013). Tsunamigenic earthquakes in the Gulf of Cadiz: fault model and recurrence. *Natural Hazards and Earth System Sciences*, *13*(1), 1–13. doi: 10.5194/nhess-13-1-2013

Medialdea, T., Somoza, L., Pinheiro, L., Fernández-Puga, M., Vázquez, J., León, R., ... Vegas, R. (2009). Tectonics and mud volcano development in the Gulf of Cádiz. *Marine Geology*, *261*(1-4), 48–63. doi: 10.1016/j.margeo.2008.10.007

Moscardelli, L., & Wood, L. (2008). New classification system for mass transport complexes in offshore Trinidad. *Basin Research*, *20*(1), 73–98. doi: 10.1111/j.1365-2117.2007.00340.x

Moser, T., & Howard, C. (2008). Diffraction imaging in depth. *Geophysical Prospecting*, *56*(5), 627–641. doi: 10.1111/j.1365-2478.2007.00718.x

Mulder, T., & Cochonat, P. (1996). Classification of offshore mass movements. *Journal of Sedimentary Research*, *66*(1), 43–57. doi: 10.1306/D42682AC-2B26-11D7-8648000102C1865D

Piper, D. J. W., Cochonat, P., & Morrison, M. L. (1999). The sequence of events around the epicentre of the 1929 Grand Banks earthquake: initiation of debris flows and turbidity current inferred from sidescan sonar. *Sedimentology*, *46*(1), 79–97. doi: 10.1046/j.1365-3091.1999.00204.x

Piper, D. J. W., Pirmez, C., Manley, P. L., Long, D., Flood, R. D., Normark, W. R., & Showers, W. (1997). Mass-transport deposits of the Amazon fan. *Proceedings of the Ocean Drilling Program. Scientific results*, *155*, 109–146.

Posamentier, H. W., Martinsen, O. J., & Shipp, R. (2011). The character and genesis of submarine mass-transport deposits: insights from outcrop and 3D seismic data. *Mass-transport deposits in deepwater settings. Tulsa: SEPM, Special Publication*, *96*, 7–38.

Prior, D. B., Bornhold, B. D., & Johns, M. W. (1984). Depositional Characteristics of a Submarine Debris Flow. *The Journal of Geology*, *92*(6), 707–727. doi: 10.1086/628907

Randen, T., & Sønneland, L. (2005). Atlas of 3D Seismic Attributes. In H.-G. Bock et al. (Eds.), *Mathematical Methods and Modelling in Hydrocarbon Exploration and Production* (Vol. 7, pp. 23–46). Berlin, Heidelberg: Springer Berlin Heidelberg. doi: 10.1007/3-540-26493-0_2

Reshef, M., & Landa, E. (2009). Post-stack velocity analysis in the dip-angle domain using diffractions. *Geophysical Prospecting*, *57*(5), 811–821. doi: 10.1111/j.1365-2478.2008.00773.x

Satake, K. (2012). Tsunamis Generated by Submarine Landslides. In Y. Yamada et al. (Eds.), *Submarine Mass Movements and Their Consequences* (pp. 475–484). Dordrecht: Springer Netherlands. doi: 10.1007/978-94-007-2162-3_42

Sawyer, D. E., Flemings, P. B., Dugan, B., & Germaine, J. T. (2009). Retrogressive failures recorded in mass transport deposits in the Ursa Basin, Northern Gulf of Mexico. *Journal of Geophysical Research: Solid Earth*, *114*(B10). doi: 10.1029/2008JB006159

Schwarz, B. (2019). Coherent wavefield subtraction for diffraction separation. *GEOPHYSICS*, *84*(3), V157–V168. doi: 10.1190/geo2018-0368.1

Shipp, R. C., Nott, J. A., & Newlin, J. A. (2004). Physical Characteristics and Impact of Mass Transport Complexes on Deepwater Jetted Conductors and Suction Anchor Piles. In *Offshore Technology Conference.* Houston, Texas: Offshore Technology Conference. doi: 10.4043/16751-MS

Sobiesiak, M. S., Alsop, G. I., Kneller, B., & Milana, J. P. (2017). Sub-seismic scale folding and thrusting within an exposed mass transport deposit: A case study from NW Argentina. *Journal of Structural Geology*, *96*, 176–191. doi: 10.1016/j.jsg.2017.01.006

Steventon, M. J., Jackson, C. A.-L., Hodgson, D. M., & Johnson, H. D. (2019). Strain analysis of a seismically imaged mass-transport complex, offshore Uruguay. *Basin Research*, *31*(3), 600–620. doi: 10.1111/bre.12337

Stolt, R. H. (1978). Migration by Fourier transform. *GEOPHYSICS*, *43*(1), 23–48. doi: 10.1190/1.1440826

Tappin, D. R., Watts, P., McMurtry, G. M., Lafoy, Y., & Matsumoto, T. (2001). The Sissano, Papua New Guinea tsunami of July 1998 — offshore evidence on the source mechanism. *Marine Geology*, *175*(1), 1–23. doi: 10.1016/S0025-3227(01)00131-1

Terrinha, P., Pinheiro, L., Henriet, J.-P., Matias, L., Ivanov, M., Monteiro, J., ... Rovere, M. (2003). Tsunamigenic-seismogenic structures, neotectonics, sedimentary processes and slope instability on the southwest Portuguese Margin. *Marine Geology*, *195*(1-4), 55–73. doi: 10.1016/S0025-3227(02)00682-5

Urgeles, R., & Camerlenghi, A. (2013). Submarine landslides of the Mediterranean Sea: Trigger mechanisms, dynamics, and frequency-magnitude distribution. *Journal of Geophysical Research: Earth Surface*, *118*(4), 2013JF002720. doi: 10.1002/2013JF002720

Urgeles, R., INSIGHT Leg 2 cruise shipboard participants, & . (2019). *ImagiNg large SeismogenIc and tsunamiGenic structures of the Gulf of Cadiz with ultra-High resolution Technologies (INSIGHT) Leg 2 survey cruise report* (Tech. Rep.). Institute of Marine Sciences, Barcelona.

Vakulenko, S. A., Buryak, S. V., Gofman, P. A., & Finikov, D. B. (2014). Deghosting of High Resolution Marine Seismic Data by Adaptive Filtering Algorithm. In (Vol. 2014, pp. 1–5). European Association of Geoscientists & Engineers. doi: 10.3997/2214-4609.20142133

Vizcaino, A., Gràcia, E., Pallàs, R., Garcia-Orellana, J., Casas, D., Willmott, V., ... Asioli, A. (2006). Sedimentology, physical properties and age of mass transport deposits associated with the Marquês de Pombal Fault, Southwest Portuguese Margin. *Norwegian Journal of Geology*, 10.

Weimer, P., & Shipp, C. (2004). Mass Transport Complex: Musing on Past Uses and Suggestions for Future Directions. In *Offshore Technology Conference.* Houston, Texas: Offshore Technology Conference. doi: 10.4043/16752-MS

Yilmaz, O. (2001). *Seismic Data Analysis: Processing, Inversion, and Interpretation of Seismic Data* (2Volume Set edition ed.). Tulsa, OK: Society of Exploration Geophysicists.

Zitellini, N., Gràcia, E., Matias, L., Terrinha, P., Abreu, M., DeAlteriis, G., ... Mulder, T. (2009). The quest for the Africa–Eurasia plate boundary west of the Strait of Gibraltar. *Earth and Planetary Science Letters*, *280*(1-4), 13–50. doi: 10.1016/j.epsl.2008.12.005

Zitellini, N., Rovere, M., Terrinha, P., Chierici, F., & Matias, L. (2004). Neogene Through Quaternary Tectonic Reactivation of SW Iberian Passive Margin. *Pure and Applied Geophysics*, *161*(3), 565–587. doi: 10.1007/s00024-003-2463-4